

Article

A Framelet-based Iterative Pan-sharpening Approach

Zi-Yao Zhang, Ting-Zhu Huang ^{*}, Liang-Jian Deng ^{*}, Jie Huang, Xi-Le Zhao and Chao-Chao Zheng

School of Mathematical Sciences, University of Electronic Science and Technology of China, Chengdu, Sichuan, 611731, P. R. China

^{*} Correspondence: tzhuang@uestc.edu.cn; liangjian.deng@uestc.edu.cn

Version March 7, 2018 submitted to MDPI

Abstract: Pan-sharpening is to fuse multispectral image and panchromatic image to produce a multispectral image with high spatial resolution. In this paper, we design a new iterative method based on framelet for pan-sharpening. The proposed model takes advantage of the upsampled multispectral image and a linear relation between the panchromatic image and the latent high-resolution multispectral image. Since the sparsity of the pan-sharpened image under a B-spline framelet transform is assumed, we regularize the model by penalizing l_1 norm of a framelet based term. The model is solved by a designed algorithm based on alternating direction method of multipliers (ADMM). For better performance, we propose an iterative strategy to pick up more spectral and spatial details. Experiments on four datasets demonstrate that the proposed method outperforms several existing pan-sharpening methods.

Keywords: pan-sharpening; framelet; ADMM; iterative strategy

1. Introduction

An optical satellite usually acquires two images describing the same scene almost simultaneously, which are called multispectral (MS) image and panchromatic (PAN) image respectively. The former is a multichannel image with low spatial resolution, while the latter is a single channel image with rich spatial details. Despite the fact that MS image can be of over eight bands and the resolution of PAN image can be less than half a meter, their superiority cannot be synthesized in one image due to physical and technological constraints. However, pan-sharpening techniques are capable of creating a multichannel image with high spatial resolution out of these two images, which is of great importance for remote sensing. These techniques attract much attention of scientific community and are widely applied in many remote sensing tasks such as object recognition [1], change detection [2] and so on.

Among various pan-sharpening methods having been proposed in the literature, many of them can be put into two main categories: component substitution (CS) and multiresolution analysis (MRA). CS mainly involves three steps: firstly a spectral transformation of MS image, then a replacement of its spatial component with PAN image, and finally an inverse transformation. This class includes classical methods such as intensity-hue-saturation (IHS) [3], principal component analysis (PCA) [4], Gram-Schmidt spectral sharpening (GS) [5] and recent methods like [6] and [7]. As for MRA, it focuses on an injection process in which spatial details extracted from PAN image are added to upsampled MS image. Examples of this class include wavelet transform based methods [8–10], Laplacian Pyramid based methods [11], and methods based on other transforms [12,13].

Different from the two categories mentioned above, there are also other types of pan-sharpening methods. This family includes those based on Bayesian paradigm [14], total variation [15,16], gradient operator [17,18], sparse representation [19], super-resolution techniques [20], convolution neural network [21] and so on. Recently in [22], Deng *et al.* propose a novel variational model for pan-sharpening in which intensity function of the unknown image is considered from a continuous point of view. The related continuous function is decomposed into two components. Assumption is made that the former lies in a Reproducing Kernel Hilbert Space (RKHS) while the latter can be approximated by linear combination of approximated Heaviside functions (AHF). This

36 model outperforms several state-of-the-art pan-sharpening methods according to experiments on two datasets.
 37 However, its good performance relies on a large amount of computation, which results in rather long running
 38 time.

39 In this paper, a new iterative algorithm for pan-sharpening is proposed as an attempt to simplify RKHS
 40 method. We make use of the information from MS image by generating its upsampled form. The linear relation
 41 [22,23] between PAN image and bands of the image to be estimated is also considered in the model. A framelet
 42 based term is introduced as regularization. Besides, we adopt an iterative strategy similar to [22] to improve
 43 performance of the algorithm. The framework of the proposed approach can be seen in Figure 1. By utilizing real
 44 data from Pléiades, Quickbird, WorldView-2 and SPOT-6, we compare several existing pan-sharpening methods
 45 with the proposed method. These results show spatial and spectral fidelity of the proposed method. Meanwhile,
 46 they confirm a much less running time than RKHS method, suggesting that framelet based regularization is more
 47 mature and easier to compute.

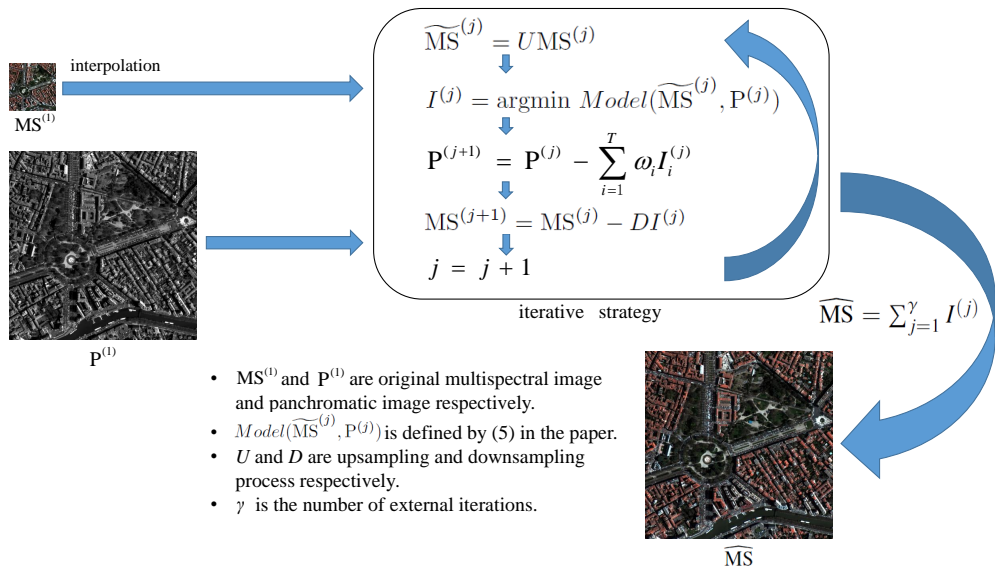


Figure 1. Framework of the proposed iterative pan-sharpening approach.

48 The rest of this paper is arranged as follows. Section II reviews the related work [22]. Then in Section III
 49 the new iterative algorithm is presented. Section IV is a display of visual and numerical experimental results
 50 together with some discussions about the proposed method. Finally, conclusion is drawn in Section V.

51 2. Related Work

52 To begin with, we introduce several notations to be used throughout this paper. Let $MS \in \mathbb{R}^{m_1 \times n_1 \times T}$ be
 53 the original multispectral image with T bands, each band denoted as $MS_i \in \mathbb{R}^{m_1 \times n_1}$. Let $\widetilde{MS} \in \mathbb{R}^{m_2 \times n_2 \times T}$ be
 54 the upsampled multispectral image, each band denoted as $\widetilde{MS}_i \in \mathbb{R}^{m_2 \times n_2}$. \widetilde{MS} represents the high-resolution
 55 multispectral image to be estimated, with $\widetilde{MS}_i \in \mathbb{R}^{m_2 \times n_2}$ being the i th band of it. Moreover, the original
 56 panchromatic image is $P \in \mathbb{R}^{m_2 \times n_2}$.

57 Deng *et al.* propose a new iterative pan-sharpening algorithm in [22], which is actually an extension of
 58 their previous work on super-resolution [24]. They view the pan-sharpening problem as an intensity estimation
 59 process for the unknown image \widetilde{MS} . The intensity of \widetilde{MS} is modelled as a hidden continuous function. It consists
 60 of two different components, a smooth one and a non-smooth one. The former is assumed to be an element of
 61 a special function space called Reproducible Kernel Hilbert Space (RKHS), while the latter is formulated as a
 62 linear combination of approximated Heaviside functions (AHF).

Specifically, let $f_i, i = 1, 2, \dots, T$, be the underlying continuous intensity function corresponding to the
 ith band of \widetilde{MS} . Without loss of generation, the domain is restricted such that $\mathbf{z} = (x, y) \in [0, 1] \times [0, 1]$. The

smooth component is decomposed as $\sum_{v=1}^M d_{v,i} \phi_{v,i}(\mathbf{z}) + \sum_{s=1}^n c_{s,i} \xi_{s,i}(\mathbf{z})$. These two series lie in two different RKHS, with $\phi_{v,i}(\mathbf{z})$, $v = 1, 2, \dots, M$, and $\xi_{s,i}(z)$, $s = 1, 2, \dots, n$, being basis functions in each RKHS respectively. $d_{v,i}$, $v = 1, 2, \dots, M$, together with $c_{s,i}$, $s = 1, 2, \dots, n$, are the corresponding coefficients. As for the non-smooth component, a family of Heaviside functions is considered to implement the approximation. However, since Heaviside functions are singular at the origin, which makes differentiation impossible to be taken there, they are approximated by a smooth form, *i.e.*, approximated Heaviside functions (AHF). In 2D case, this smooth alternative takes the form of $\psi((\cos\theta_{j,i}, \sin\theta_{j,i}) \cdot \mathbf{z} + c_{\rho,i})$, actually representing an edge with θ elevation at a location specified by $c_{\rho,i}$. It is a generalization of the 1D form $\psi(x) = \frac{1}{2} + \frac{1}{\pi} \arctan(\frac{x}{\xi})$, where ξ is a positive parameter to control smoothness. Therefore, f_i , $i = 1, 2, \dots, T$, is finally modelled as:

$$f_i = \sum_{v=1}^M d_{v,i} \phi_{v,i}(\mathbf{z}) + \sum_{s=1}^n c_{s,i} \xi_{s,i}(\mathbf{z}) + \sum_{j=1}^k \sum_{\rho=1}^n \omega_{j,i} \psi((\cos\theta_{j,i}, \sin\theta_{j,i}) \cdot \mathbf{z} + c_{\rho,i}). \quad (1)$$

63 For more details, see [22] and [24].

By evaluating on a fine grid, (1) can be discretized so that it becomes a form involving simple matrix multiplication. Let $T^h \in \mathbb{R}^{m_2 n_2 \times M}$, $K^h \in \mathbb{R}^{m_2 n_2 \times m_2 n_2}$ and $\Psi^h \in \mathbb{R}^{m_2 n_2 \times m}$ ($m = k \cdot n$) denote matrices whose entries are generated by evaluating $\phi_{v,i}(\mathbf{z})$, $\xi_{s,i}(\mathbf{z})$, and $\psi((\cos\theta_{j,i}, \sin\theta_{j,i}) \cdot \mathbf{z} + c_{\rho,i})$ on a fine grid. Then each band of the desired multichannel image with high spatial resolution can be computed as follows:

$$\widehat{\mathbf{MS}}_i = T^h \mathbf{d}_i + K^h \mathbf{c}_i + \Psi^h \mathbf{f}_i, \quad i = 1, 2, \dots, T. \quad (2)$$

Hence the pan-sharpening problem is converted into a problem of coefficient estimation. In [22], the coefficients are computed by minimizing the following model:

$$\begin{aligned} \min_{\mathbf{d}_i, \mathbf{c}_i, \beta_i} \frac{1}{N} \sum_{i=1}^T & \|T^h \mathbf{d}_i + K^h \mathbf{c}_i + \Psi^h \beta_i - \widehat{\mathbf{MS}}_i\|_2^2 + \frac{\mu}{2} \sum_{i=1}^T \mathbf{c}_i^T K^l \mathbf{c}_i + \frac{\lambda_1}{2} \sum_{i=1}^T \|\beta_i\|_1 \\ & + \frac{\lambda_2}{2} \left\| \sum_{i=1}^T \omega_i (T^h \mathbf{d}_i + K^h \mathbf{c}_i + \Psi^h \beta_i) - P \right\|_2^2, \end{aligned} \quad (3)$$

64 where N is the number of pixels that $\widehat{\mathbf{MS}}$ contains. μ , λ_1 , and λ_2 are positive parameters. $\widehat{\mathbf{MS}}_i$ is generated by an
65 upsampling process via GS method [5]. $K^l \in \mathbb{R}^{m_1 n_1 \times m_1 n_1}$ is a coarser version of K^h , *i.e.*, the discretization process
66 is done on a coarser grid. ω_i are weights reflecting the contribution of each band of $\widehat{\mathbf{MS}}$ to the linear combination
67 which approximates the panchromatic image P . This linear approximation and its variants are assumed by many
68 methods, *e.g.*, [23] and [25].

69 After the coefficients \mathbf{d}_i , \mathbf{c}_i , β_i are obtained, the high-resolution multispectral image can be computed by (2).
70 Furthermore, model (3) is combined with an iterative strategy. It will be detailed in Section III since it is used in
71 the method proposed in this paper as well.

72 3. The Proposed Method

73 Empirical results in [22] show that RKHS method outperforms several state-of-the-art pan-sharpening
74 methods both in the perspective of spatial and spectral fidelity. However, the RKHS based model of $\widehat{\mathbf{MS}}$
75 is quite complicated, since it is not easy to implement in actual calculation. In addition, the regularization
76 terms of (3) involve not only l_1 norm of β_i but also quadratic function of \mathbf{c}_i (both summed by band), which
77 adds to computational burden. As a result, the algorithm is rather time consuming. Therefore, it is natural to
78 raise a question. Can we simplify model (3) without loss of its advantage, *i.e.*, high-level spatial and spectral
79 performance? A possible way is not to make efforts to build an exquisite model of $\widehat{\mathbf{MS}}$, but seek for another
80 technique of regularization instead. This is exactly why we turn to framelet.

81 Piecewise smooth functions, for instance images, can be sparsely approximated by framelet system
82 efficiently [26]. As a result, framelet techniques are used in literature to address the problems like image
83 restoration (*e.g.*, [26], [27], and [28]). Recently, it is also applied to pan-sharpening. For instance, a framelet

⁸⁴ based MRA scheme is considered in [29]. And a framelet based variational model consists of four parts, each
⁸⁵ related to an assumption, is introduced in [30]. They are able to obtain good results. Nevertheless, in this section,
⁸⁶ we consider a combination of variational model and iterative strategy instead of building a complicated model,
⁸⁷ *i.e.*, we try to build a simple framelet based variational model and then combine it with an iterative strategy to
⁸⁸ yield a novel and effective approach for pan-sharpening.

In discrete case, let W and W^T denote fast framelet decomposition and construction respectively. They are constructed by unitary extension principle (UEP) [31], and satisfy the relation $W^T W = I$. In this paper, we use the piecewise linear B-spline framelets [26]. An L -level framelet transform of an image u [26] can be denoted as:

$$Wu = \{W_{l,j}u, 0 \leq l \leq L-1, j \in \mathcal{I}\}, \quad (4)$$

⁸⁹ where $W_{l,j}u$ denotes the coefficients of u in framelet band j at level l under the framelet transform, and \mathcal{I} is the
⁹⁰ index set of all framelet bands. Throughout this paper, we empirically set $L = 1$. For more theoretical details of
⁹¹ framelet, see *e.g.*, [32].

Consequently, by employing framelet based regularization, (3) can be modified. Each band of $\widehat{\text{MS}}$ is computed by minimizing the following function:

$$\min_{\widehat{\text{MS}}_i} \frac{1}{2} \sum_{i=1}^T \|\widehat{\text{MS}}_i - \widetilde{\text{MS}}_i\|_2^2 + \frac{\alpha}{2} \left\| \sum_{i=1}^T \omega_i \widehat{\text{MS}}_i - P \right\|_2^2 + \sum_{i=1}^T \|\lambda_i \cdot W(\widehat{\text{MS}}_i)\|_1, \quad (5)$$

⁹² where α and λ_i are parameters. Dot product is used in the third term since there are more than one framelet band,
⁹³ as (4) suggested. Coefficients for bands of $\widehat{\text{MS}}$, *i.e.*, ω_i , and are estimated automatically by a linear regression [23]
⁹⁴ between the original multispectral image and downsampled panchromatic image. The upsampled multispectral
⁹⁵ image $\widehat{\text{MS}}_i$ is generated via GS method. Note that this model can also be viewed as an extension of the so-called
⁹⁶ analysis based model for image restoration (*e.g.*, [33] and [34]). Each l_1 term of (5) is in accordance with that
⁹⁷ defined in the analysis based model. Concretely, it can be expressed as

$$\|\lambda_i \cdot W(\widehat{\text{MS}}_i)\|_1 = \left\| \sum_{j \in \mathcal{I}} \lambda_{i,j} |W_{i,j}(\widehat{\text{MS}}_i)| \right\|_1. \quad (6)$$

⁹⁸ This expression is the case where 1-level framelet transform is imposed on $\widehat{\text{MS}}_i$, as we emphasized above.

Model (5) can be solved by methods such as primal-dual method [35] and ADMM [36] efficiently. We choose ADMM here, whose application covers a wide range of image processing, such as image denoising [37], image super-resolution [38], tensor completion [39] and so on. Its convergence is guaranteed by many works such as [40] and [41]. Due to non-smoothness caused by l_1 term, the first step is to rewrite (5) as an equivalent form through substitution of variables:

$$\begin{aligned} & \min_{u_i, V_i, \widehat{\text{MS}}_i} \frac{1}{2} \sum_{i=1}^T \|\widehat{\text{MS}}_i - \widetilde{\text{MS}}_i\|_2^2 + \frac{\alpha}{2} \left\| \sum_{i=1}^T \omega_i V_i - P \right\|_2^2 + \sum_{i=1}^T \|\lambda_i \cdot u_i\|_1 \\ & \text{s.t., } u_i = W(\widehat{\text{MS}}_i), V_i = \widehat{\text{MS}}_i, i = 1, \dots, T. \end{aligned} \quad (7)$$

Then we can obtain the augmented Lagrangian of (7), *i.e.*,

$$\begin{aligned} \mathcal{L}(\widehat{\text{MS}}_i, u_i, V_i, D_i, E_i) = & \frac{1}{2} \sum_{i=1}^T \|\widehat{\text{MS}}_i - \widetilde{\text{MS}}_i\|_2^2 + \frac{\alpha}{2} \left\| \sum_{i=1}^T \omega_i V_i - P \right\|_2^2 + \sum_{i=1}^T \|\lambda_i \cdot u_i\|_1 \\ & + \frac{\beta_2}{2} \sum_{i=1}^T \|u_i - W(\widehat{\text{MS}}_i)\|_2^2 + \sum_{i=1}^T E_i^T (u_i - W(\widehat{\text{MS}}_i)) \\ & + \frac{\beta_1}{2} \sum_{i=1}^T \|V_i - \widehat{\text{MS}}_i\|_2^2 + \sum_{i=1}^T D_i^T (V_i - \widehat{\text{MS}}_i), \end{aligned} \quad (8)$$

99 where D_i and E_i are Lagrangian multipliers, β_1 and β_2 are two positive parameters.

100 Now we denote $F_i = D_i/\beta_1$ and $G_i = E_i/\beta_2$. According to ADMM, problem (7) can be solved by
101 implementing the following iterative scheme:

1) For $i = 1, \dots, T$, update each $u_i^{(k)}$ by solving:

$$u_i^{(k+1)} = \arg \min_{u_i} \|\lambda_i \cdot u_i\|_1 + \frac{\beta_2}{2} \|u_i - W(\widehat{\text{MS}}_i^{(k)}) + G_i^{(k)}\|_2^2. \quad (9)$$

2) For $i = 1, \dots, T$, update each $V_i^{(k)}$ by solving:

$$V_i^{(k+1)} = \arg \min_{V_i} \frac{\alpha}{2} \left\| \sum_{1 \leq j < i} \omega_j V_j^{(k+1)} + \omega_i V_i + \sum_{i < j \leq T} \omega_j V_j^{(k)} - P \right\|_2^2 + \frac{\beta_1}{2} \|V_i - \widehat{\text{MS}}_i^{(k)} + F_i^{(k)}\|_2^2. \quad (10)$$

3) For $i = 1, \dots, T$, update each $\widehat{\text{MS}}_i^{(k)}$ by solving:

$$\begin{aligned} \widehat{\text{MS}}_i^{(k+1)} = \arg \min_{\widehat{\text{MS}}_i} \frac{1}{2} \|\widehat{\text{MS}}_i - \widehat{\text{MS}}_i^{(k)}\|_2^2 + \frac{\beta_1}{2} \|V_i^{(k+1)} - \widehat{\text{MS}}_i + F_i^{(k)}\|_2^2 \\ + \frac{\beta_2}{2} \|u_i^{(k+1)} - W(\widehat{\text{MS}}_i) + G_i^{(k)}\|_2^2. \end{aligned} \quad (11)$$

4) For $i = 1, \dots, T$, update each $F_i^{(k)}$ by $F_i^{(k+1)} = F_i^{(k)} + (V_i^{(k+1)} - \widehat{\text{MS}}_i^{(k+1)})$.

5) For $i = 1, \dots, T$, update each $G_i^{(k)}$ by $G_i^{(k+1)} = G_i^{(k)} + (u_i^{(k+1)} - W(\widehat{\text{MS}}_i^{(k+1)}))$.

102 Note that (9)-(11) have closed-form solutions. Using soft-thresholding operator (e.g., [42]) \mathcal{T}_τ , $u_i^{(k+1)}$ can
103 be rewritten as:

$$u_i^{(k+1)} = \mathcal{T}_{\lambda_i/\beta_2}(W(\widehat{\text{MS}}_i^{(k)}) - G_i^{(k)}), \quad (12)$$

104 where $\mathcal{T}_\tau(v)$ is defined entry-wise by

$$\mathcal{T}_\tau(v) = \frac{\nu}{|v|} \max\{|v| - \tau, 0\}, \quad (13)$$

As for (10) and (11), they can be solved easily as follows:

$$V_i^{(k+1)} = \frac{\alpha \omega_i (P - \sum_{1 \leq j < i} \omega_j V_j^{(k+1)} - \sum_{i < j \leq T} \omega_j V_j^{(k)}) + \beta_1 (\widehat{\text{MS}}_i^{(k)} - F_i^{(k)})}{\alpha \omega_i^2 + \beta_1}, \quad (14)$$

$$\widehat{\text{MS}}_i^{(k+1)} = \frac{\widehat{\text{MS}}_i + \beta_1 (V_i^{(k+1)} + F_i^{(k)}) + \beta_2 W^T (u_i^{(k+1)} + G_i^{(k)})}{\beta_1 + \beta_2 + 1}. \quad (15)$$

106 In order to facilitate illustration of the proposed algorithm, we summarize these steps of ADMM as
107 Algorithm 1. Note that for simplicity of form, we write each iteration of ADMM in Algorithm 1 in an order
108 slightly different from what we mentioned above, but it is easy to validate that they give the same results.

Algorithm 1

Input: panchromatic image P , upsampled multispectral image \widehat{MS} , $\omega_i \alpha, \lambda_i, \beta_1, \beta_2$.
Output: high-resolution multispectral image \widehat{MS} .

```

while not converged do
    for  $i = 1 : T$  do
        1) Solve  $u_i^{(k+1)}$  by (12).
        2) Solve  $V_i^{(k+1)}$  by (14).
        3) Solve  $\widehat{MS}_i^{(k+1)}$  by (15).
        4) Update  $F_i^{(k)}$  by  $F_i^{(k+1)} = F_i^{(k)} + (V_i^{(k+1)} - \widehat{MS}_i^{(k+1)})$ .
        5) Update  $G_i^{(k)}$  by  $G_i^{(k+1)} = G_i^{(k)} + (u_i^{(k+1)} - W(\widehat{MS}_i^{(k+1)}))$ .
    end for
end while

```

109 Although Algorithm 1 itself is a complete algorithm, there is still room for improvement. Thus an iterative
110 strategy is considered. For accordance of notations, let $P^{(1)} = P$ and $MS^{(1)} = MS$. Similarly, denote the
111 first output of Algorithm 1 as $I^{(1)}$. After obtaining \widehat{MS} , we compute $P^{(2)} = P - \sum_{i=1}^T \omega_i \widehat{MS}_i$. In addition, let
112 $\widehat{MS}^{(2)} = U(MS - D(\widehat{MS}))$. D represents a downsampling operator, and U represents the upsampling process
113 by which \widehat{MS} is generated. Now we view $P^{(2)}$ and $\widehat{MS}^{(2)}$ as new inputs for Algorithm 1 instead of the original
114 P and \widehat{MS} . The resulting new output can be denoted as $I^{(2)}$. By repeating this strategy, we obtain a series of
115 $I^{(j)}, j = 2, 3, \dots, \gamma$. Then the sum of all $I^{(j)}, j = 1, 2, \dots, \gamma$, is taken as the final high-resolution multichannel
116 image. This iterative strategy is adopted in not only pan-sharpening [22] but also image super-resolution [24].

117 Now we can summarize the procedures above as Algorithm 2:

Algorithm 2 The proposed iterative pan-sharpening algorithm

Input: panchromatic image P , multispectral image MS , $\omega_i \alpha, \lambda_i, \beta_1, \beta_2$.
Output: high-resolution multispectral image \widehat{MS} .

```

1. Initialization:  $MS^{(1)} = MS, P^{(1)} = P$ .
for  $j = 1 : \gamma$  do
    1) Upsample  $MS^{(j)}$  to obtain  $\widehat{MS}^{(j)}$ .
    2) Compute  $I^{(j)}$  by implementing Algorithm 1 ( $\widehat{MS}^{(j)}, P^{(j)}$  instead of  $\widehat{MS}, P$  as input).
    3) Update  $P^{(j)}$  by  $P^{(j+1)} = P^{(j)} - \sum_{i=1}^T \omega_i I_i^{(j)}$ .
    4) Update  $MS^{(j)}$  by  $MS^{(j+1)} = MS^{(j)} - D(I^{(j)})$ .
end for
2. Compute the final output:  $\widehat{MS} = \sum_{j=1}^{\gamma} I^{(j)}$ .

```

118 Note that γ is the number of outer iterations. The downsampling process D in each iteration is completed
119 through a combination of two steps: compute the modulation transfer function of $I^{(j)}$ with Gaussian filter and
120 then interpolate it to the size of MS in a "nearest" way [22]. And the upsampling process is done by GS method.

4. Results and Discussion

122 In this section, we firstly utilize four datasets to compare the proposed method with several pan-sharpening
123 methods. After that, discussions related to the number of outer iterations of Algorithm 2 are made. Results about
124 time cost are presented as well.

125 The tested datasets are acquired by Quickbird (4 bands, 512×512), Pléiades (4 bands, 1024×1024),
126 WorldView-2 (4 bands, 800×800), and SPOT-6 (4 bands, 1024×1024). The dataset of Quickbird can be
127 downloaded from <http://glcf.umd.edu/data/quickbird/chilika.shtml>. And the dataset of Pléiades is downloaded
128 together with the source codes of [43] from <http://openremotesensing.net/knowledgebase/quality-assessment-of>

pan-sharpening-methods-in-high-resolution-satellite-images-using-radiometric-and-geometric-index/. As for datasets of WorldView-2 and SPOT-6, we download them from <http://cms.mapmart.com/Samples.aspx>.

Since high resolution multispectral images are not available in the datasets, we follow Wald's protocol [44]. Therefore, the original multispectral images in the datasets are treated as ground truth. The scale ratio is 4, thus the simulated low-resolution multispectral images (4 bands) are of the size 128×128 , 256×256 , 200×200 , and 256×256 respectively. Each of them is downsampled from the corresponding ground truth in the same way as that in Algorithm 2, *i.e.*, filter the ground truth by a Gaussian filter matched with the modulation transfer function (MTF) and then downscale it by "nearest" interpolation. As for each P, it is generated by combining bands of the ground truth linearly.

Parameters of the proposed algorithm are empirically set as follows. We use 1-level piecewise linear B-spline framelet. For each band, λ_i is equally set as:

$$\lambda_i = 10^{-4} \begin{pmatrix} 0 & 1 & 1 \\ 1 & 1 & 1 \\ 1 & 1 & 1 \end{pmatrix}. \quad (16)$$

Other model parameters in (8) are set as $\alpha = 1.5$, $\beta_1 = 0.5$, and $\beta_2 = 0.5$, with coefficients ω_i estimated by linear regression. In addition, the number of the external iterations in Algorithm 2, *i.e.*, γ , is set as 5. For different datasets, these settings may not always be the best choice, but we unify them to display stability of the proposed method and also to save efforts of tuning.

Methods compared with the proposed method comprise some classical pan-sharpening methods (PCA [4], GS [5], HPF [45], and MTFGLP [46]+ [47]) and different kinds of recent state-of-the-art methods (PHLP [48], NIHS [49], and RKHS [22]). All the experiments are conducted in MATLAB on a laptop with 4GB RAM and 1.70GHz Intel(R) Core(TM) i5-4210U CPU.

4.1. Visual Comparison

Figure 2 to Figure 5 show visual results obtained by conducting experiments on four datasets aforementioned. Each set of figures contains output images produced by eight different methods. Each ground truth is also presented as reference. For better visualization, we show local enlarged images at the bottom-left corner of each output image.

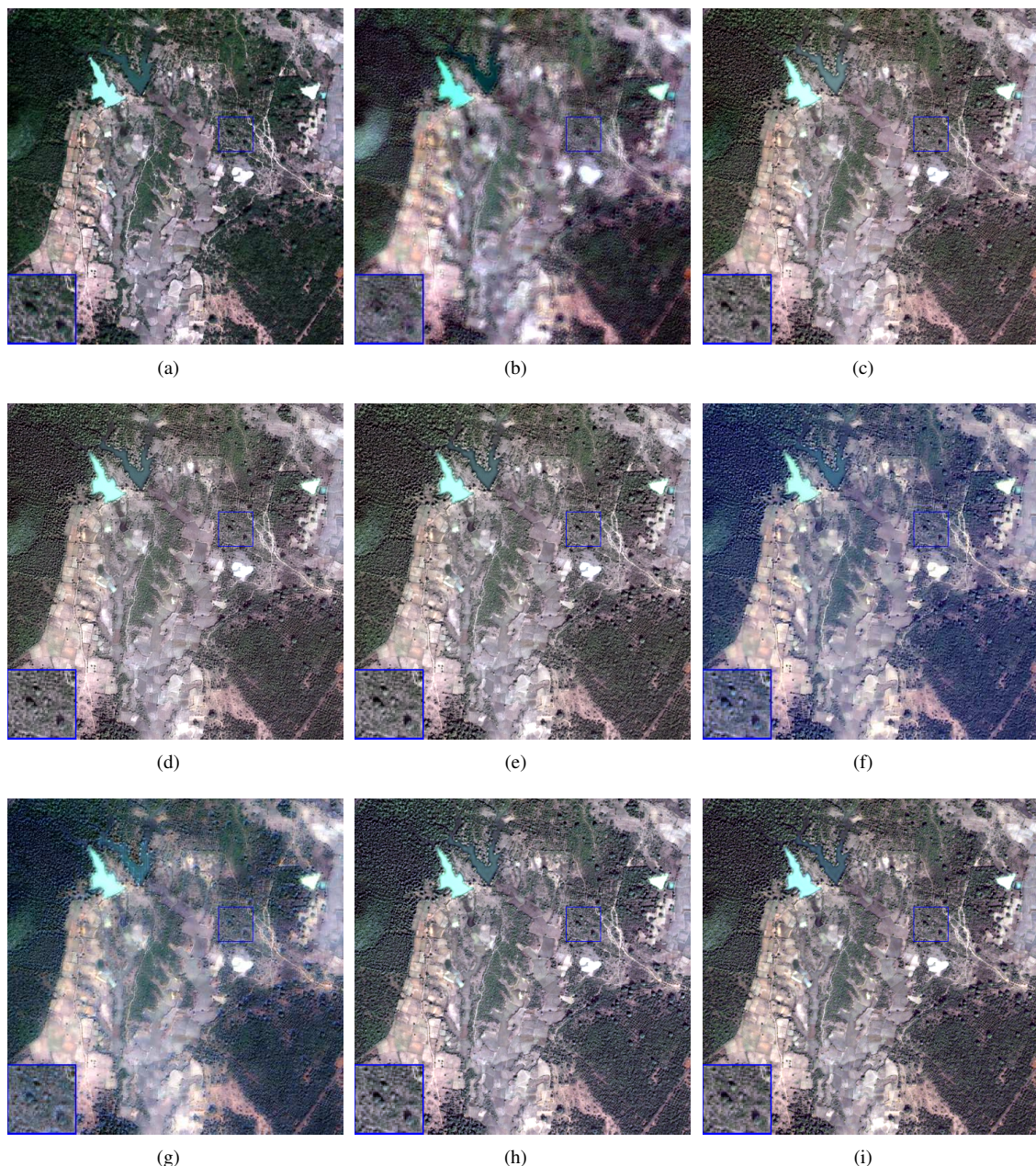


Figure 2. Visual results for Quickbird dataset (4 bands, 512×512) obtained by different pan-sharpening methods.
(a) Referential high resolution multispectral image, **(b)** PCA method, **(c)** GS method, **(d)** HPF method, **(e)** MTFGLP method, **(f)** PHLIP method, **(g)** NIHS method, **(h)** RKHS method, **(i)** Proposed method.

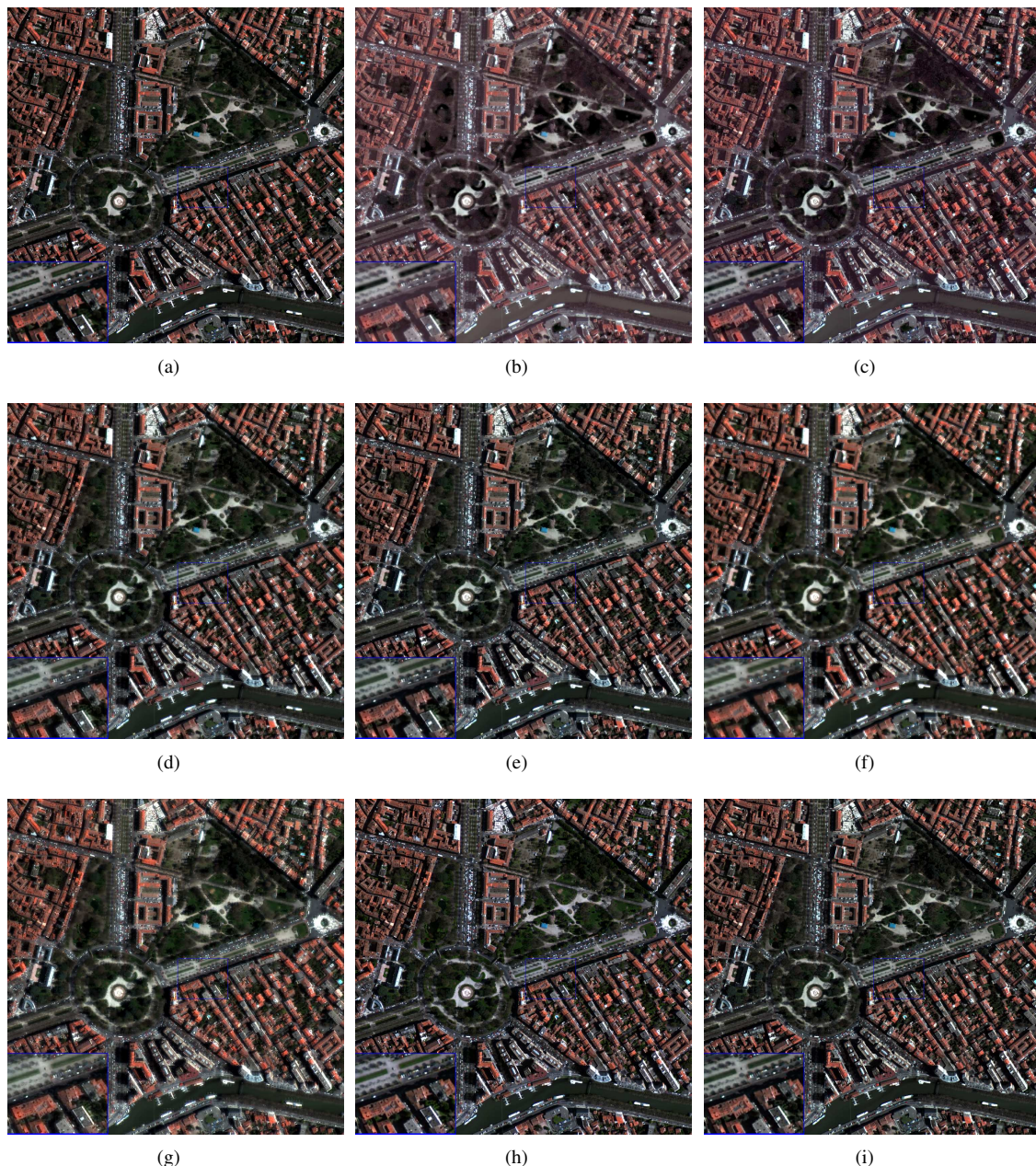


Figure 3. Visual results for Pléiades dataset (4 bands, 1024×1024) obtained by different pan-sharpening methods. (a) Referential high resolution multispectral image, (b) PCA method, (c) GS method, (d) HPF method, (e) MTFGLP method, (f) PHLP method, (g) NIHS method, (h) RKHS method, (i) Proposed method.

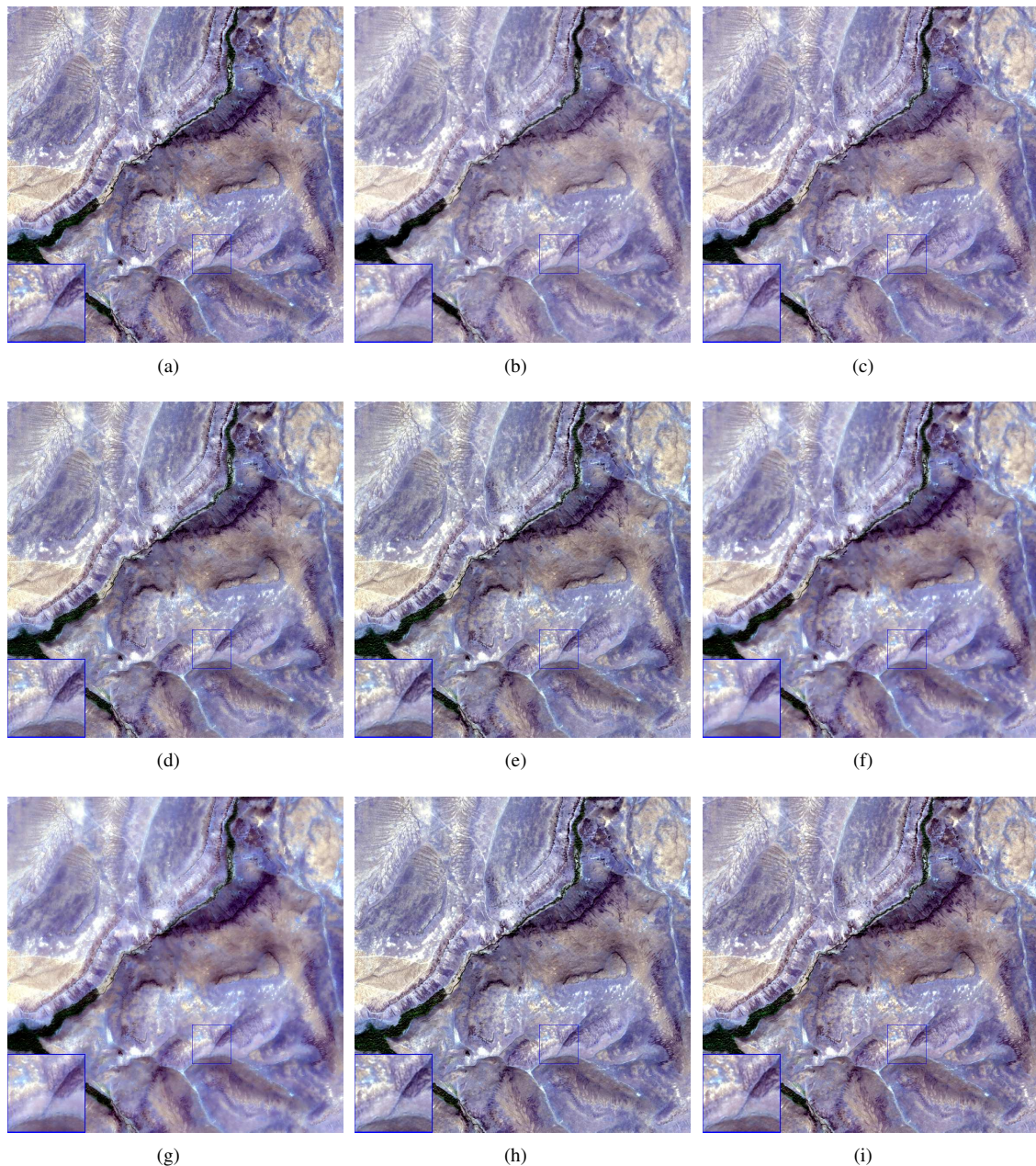


Figure 4. Visual results for WorldView-2 dataset (4 bands, 800×800) obtained by different pan-sharpening methods. (a) Referential high resolution multispectral image, (b) PCA method, (c) GS method, (d) HPF method, (e) MTFGLP method, (f) PHLP method, (g) NIHS method, (h) RKHS method, (i) Proposed method.

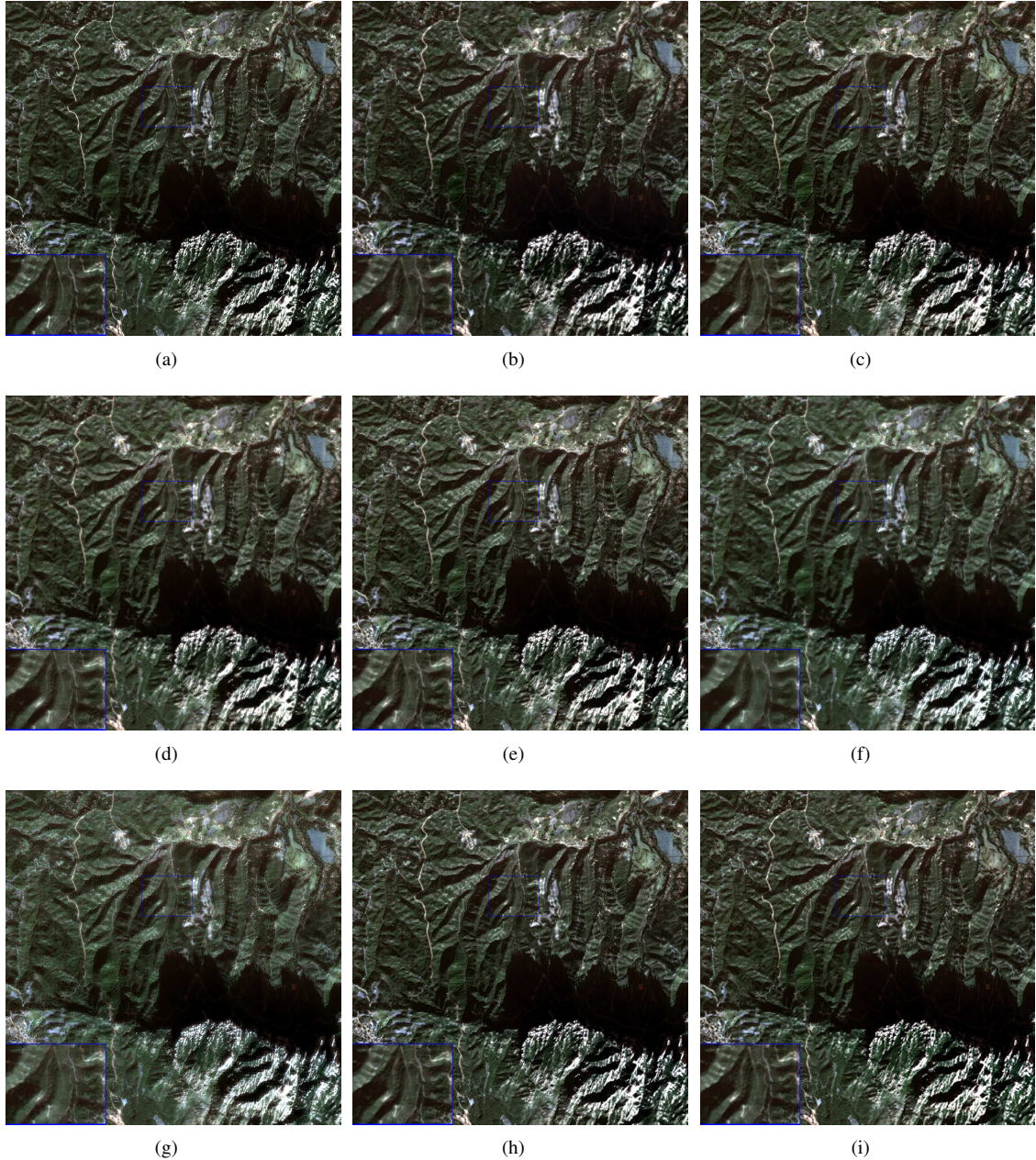


Fig. 5. Visual results of the SPOT-6 dataset (4 bands, 1024×1024) obtained by different pan-sharpening methods.
 (a) Referential high resolution multispectral image, (b) PCA method, (c) GS method, (d) HPF method, (e) MTFGLP method, (f) PHLIP method, (g) NIHS method, (h) RKHS method, (i) Proposed method.

It is obvious that all of the rest methods perform better than PCA method both in terms of spatial quality and spectral fidelity according to Figure 2 to Figure 4. GS method outperforms PCA method significantly but generally fails to avoid great spectral distortion, which is most visible on Quickbird dataset and Pléiades dataset. NIHS method and PHLIP method preserve spectral characteristics quite well. However, from the perspective of spatial details, they tend to generate excessive smooth results, thus the pan-sharpened images provided by them lack much sharp spatial information compared with the reference images.

HPF method and MTFGLP method are visually without much spectral distortion and are able to keep more spatial details. However, a closer look at their resulting images, *e.g.*, in Figure 3, suggests that they are not able to provide as many spatial details as the proposed method does. Finally, it is noticeable that RKHS method and the proposed method achieve the best visual performance on the last three experimented datasets. Actually,

visual comparisons show little disparity for these four methods. However, we will demonstrate that the proposed method gives the best quantitative results in section 4.2.

4.2. Quantitative Comparison

Several quantitative indices are employed to report the performance of different pan-sharpening methods. To evaluate spectral distortion, we use spectral angle mapper (SAM) [50], erreur relative globale adimensionnelle de synthèse (ERGAS) [50], universal image quality index (Q) [51] together with its vector extension Q4 [52], and relative average spectral error (RASE) [53] (the larger Q and Q4 and the smaller SAM and ERGAS, the better performance). Correlation coefficient (CC) [54], with 1 being its ideal value, acts as spatial quality metric. Meanwhile, we use peak signal-to-noise ratio (PSNR) and root mean square error (RMSE) as metrics of fusion accuracy. Generally speaking, better performance is achieved when PSNR is larger and RMSE is smaller.

In each experiment, most of the compared methods require an upsampled multispectral image as an input. Unless specially specified in the literature, we uniformly generate them by interpolating via a kernel function which is a polynomial with 23 coefficients [55].

Table 1. Quantitative results for Quickbird dataset.

Method	SAM	Q4	Q	RASE	ERGAS	CC	RMSE	PSNR
PCA	5.2812	0.7734	0.3895	21.5874	4.7453	0.7520	0.1246	18.0910
GS	2.3162	0.8510	0.8345	12.3841	2.9310	0.9433	0.0715	22.9177
HPF	2.1727	0.8561	0.8299	8.5465	2.0681	0.9420	0.0493	26.1392
MTFGLP	2.2767	0.8756	0.8399	6.1273	1.6287	0.9439	0.0354	29.0296
PHLP	5.0053	0.8184	0.7736	11.5526	2.9020	0.9077	0.0667	23.5214
NIHS	2.9060	0.7212	0.7521	14.4955	3.4247	0.9161	0.0837	21.5503
RKHS	3.0682	0.8725	0.8380	7.4955	1.9868	0.9413	0.0433	27.2789
Proposed	2.2422	0.8816	0.8525	5.1265	1.4605	0.9484	0.0296	30.5785

Table 2. Quantitative results for Pléiades dataset.

Method	SAM	Q4	Q	RASE	ERGAS	CC	RMSE	PSNR
PCA	9.5457	0.7829	0.8387	32.8033	8.0507	0.9276	0.0637	23.9147
GS	9.1222	0.8336	0.8900	28.8060	6.4917	0.9645	0.0560	25.0434
HPF	10.8694	0.8376	0.9243	27.8449	6.7583	0.9722	0.0541	25.3382
MTFGLP	4.7925	0.9063	0.9653	14.6515	3.2470	0.9801	0.0285	30.9155
PHLP	3.9558	0.7749	0.9186	23.6349	4.8308	0.9508	0.0459	26.7620
NIHS	5.8053	0.7807	0.8954	32.9408	6.6098	0.9500	0.0640	23.8784
RKHS	3.8294	0.9071	0.9710	12.0542	2.5088	0.9829	0.0234	32.6103
Proposed	3.2465	0.9278	0.9775	10.3886	2.1452	0.9857	0.0202	33.9019

Table 3. Quantitative results for WorldView-2 dataset.

Method	SAM	Q4	Q	RASE	ERGAS	CC	RMSE	PSNR
PCA	7.1137	0.9256	0.9137	17.4524	3.9960	0.9608	0.0778	22.1796
GS	5.2254	0.9312	0.9438	13.1991	3.2049	0.9776	0.0588	24.6058
HPF	4.1352	0.9185	0.9487	9.9563	2.4925	0.9832	0.0444	27.0547
MTFGLP	4.3926	0.9372	0.9531	9.1386	2.3852	0.9857	0.0407	27.7991
PHLP	4.0716	0.7879	0.9058	13.5540	3.2978	0.9720	0.0604	24.3753
NIHS	1.7128	0.7751	0.8781	29.6650	5.6749	0.9645	0.1323	17.5718
RKHS	5.3524	0.9340	0.9546	11.7716	2.9588	0.9864	0.0525	25.6000
Proposed	3.5176	0.9441	0.9647	6.6818	1.7829	0.9879	0.0298	30.5188

Table 4. Quantitative results for SPOT-6 dataset.

Method	SAM	Q4	Q	RASE	ERGAS	CC	RMSE	PSNR
PCA	8.4179	0.8594	0.9002	23.3863	6.1677	0.9653	0.0565	24.9547
GS	7.0558	0.8976	0.9248	25.6653	5.2751	0.9804	0.0620	24.1470
HPF	7.7539	0.8707	0.9172	26.0012	5.5211	0.9727	0.0628	24.0340
MTFGLP	3.8118	0.9162	0.9362	20.5174	4.1687	0.9795	0.0496	26.0915
PHLP	5.8827	0.7768	0.9044	21.1517	4.8940	0.9659	0.0511	25.8270
NIHS	3.8008	0.7848	0.8770	34.3983	6.4343	0.9588	0.0831	21.6032
RKHS	2.5938	0.9266	0.9530	11.8152	2.8106	0.9842	0.0286	30.8851
Proposed	3.2818	0.9300	0.9566	10.8640	2.6335	0.9843	0.0263	31.6141

The quantitative results of four datasets with regard to eight metrics are reported in Table 1 to Table 4. They clearly validate that the rest of the methods outperform PCA method as visual comparison in section 4.1 preliminarily confirmed. GS method maintain spectral fidelity well on Quickbird dataset and WorldView-2 dataset, while on the rest two datasets it performs not so well. Compared with methods such as MTFGLP method and HPF method, PHLP method and NIHS method give comparable results with respect to SAM. However, there is still gap when it comes to metrics reflecting spatial quality and fusion accuracy. Similar to GS method, HPF method is unable to preserve enough characteristics on Pléiades dasaset and SPOT-6 dataset from a spectral point of view. If not taking the proposed method into consideration, RKHS method or MTFGLP method performs the best. However, the proposed method consistently achieves better quantitative performance than them in terms of all metrics (except for SAM) on the four tested datasets. These observations are sufficient to demonstrate that the proposed method preserves spectral information and sharp spatial details accurately.

4.3. Discussion on the number of outer iterations

In Algorithm 2, we use an iterative strategy to improve the performance of Algorithm 1. The number of this outer iterations, *i.e.*, γ , is set to 5. It is meaningful to inspect how the performance of Algorithm 2 changes as γ increases.

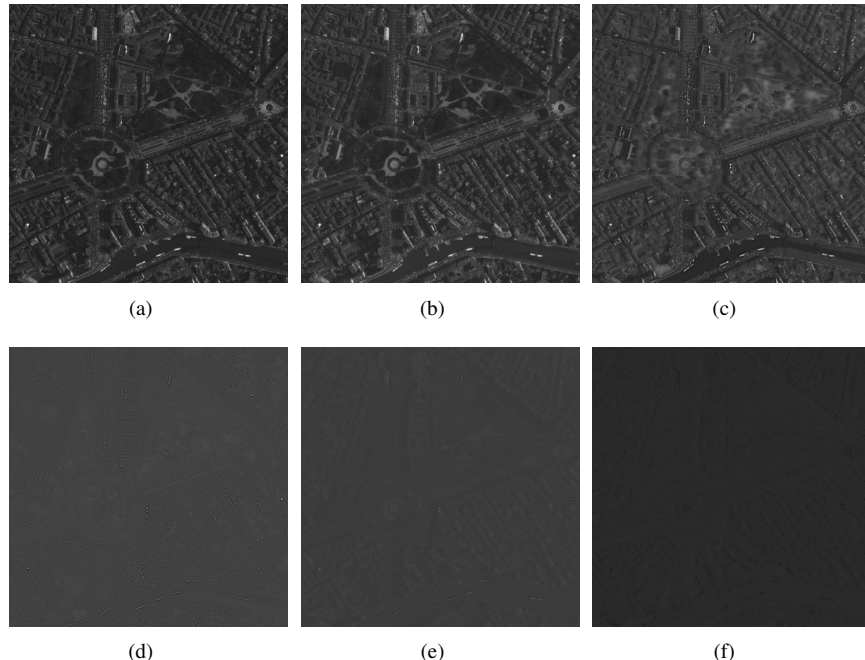


Figure 6. $I^{(j)}$ computed by Algorithm 2 for Pléiades dataset; (a) the first channel of the sum of $I^{(j)}$, $j = 1, 2, 3, 4, 5$; (b) the first channel of $I^{(1)}$; (c) the first channel of $I^{(2)}$; (d) the first channel of $I^{(3)}$; (e) the first channel of $I^{(4)}$; (f) the first channel of $I^{(5)}$.

In Figure 6, we present $I^{(j)}$, $j = 1, 2, 3, 4, 5$, each being the result of the j th outer iteration of Algorithm 2 with respect to Pléiades dataset. To focus on spatial details, only the first channel of each image is shown. For each of the last four images, we subtract its intensities by the corresponding smallest value in the channel before normalization, since these images contain negative intensities which cannot be plotted by MATLAB directly. For better visualization, the normalization of these four images are implemented by dividing the largest intensity of $I^{(2)}$ since their absolute values are rather small compared with $I^{(1)}$. From these visual results, we know that the outer iteration in Algorithm 2 is able to pick up more image details.

Table 5. Quantitative results for Quickbird dataset with different numbers of outer iterations.

Case	SAM	Q4	Q	RASE	ERGAS	CC	RMSE	PSNR
$\gamma = 1$	3.6036	0.8633	0.8274	10.0852	2.5146	0.9393	0.0582	24.7013
$\gamma = 2$	2.6197	0.8796	0.8468	6.3718	1.6839	0.9471	0.0368	28.6898
$\gamma = 3$	2.2813	0.8816	0.8499	5.4827	1.5165	0.9476	0.0316	29.9951
$\gamma = 4$	2.3563	0.8828	0.8496	5.2938	1.5354	0.9465	0.0306	30.2996
$\gamma = 5$	2.2422	0.8816	0.8525	5.1265	1.4605	0.9484	0.0296	30.5785
$\gamma = 6$	2.3382	0.8822	0.8500	5.1863	1.5145	0.9465	0.0299	30.4778

Table 6. Quantitative results for Pléiades dataset with different numbers of outer iterations.

Case	SAM	Q4	Q	RASE	ERGAS	CC	RMSE	PSNR
$\gamma = 1$	5.8470	0.8758	0.9383	19.2451	4.1779	0.9754	0.0374	28.5467
$\gamma = 2$	3.5671	0.9187	0.9725	11.8189	2.4454	0.9830	0.0230	32.7816
$\gamma = 3$	3.4947	0.9244	0.9746	11.5754	2.3527	0.9839	0.0225	32.9624
$\gamma = 4$	4.1877	0.9247	0.9731	12.5506	2.5343	0.9843	0.0244	32.2598
$\gamma = 5$	3.2465	0.9278	0.9775	10.3886	2.1452	0.9857	0.0202	33.9019
$\gamma = 6$	3.4306	0.9275	0.9761	10.9675	2.2676	0.9854	0.0213	33.4309

Table 7. Quantitative results for WorldView-2 dataset with different numbers of outer iterations.

Case	SAM	Q4	Q	RASE	ERGAS	CC	RMSE	PSNR
$\gamma = 1$	5.2761	0.9338	0.9484	12.1816	3.0319	0.9816	0.0543	25.3026
$\gamma = 2$	4.2752	0.9422	0.9608	8.2856	2.1955	0.9872	0.0369	28.6502
$\gamma = 3$	3.7884	0.9436	0.9637	7.1468	1.8866	0.9877	0.0319	29.9344
$\gamma = 4$	3.6676	0.9439	0.9640	7.3470	1.9681	0.9878	0.0328	29.6944
$\gamma = 5$	3.5176	0.9441	0.9647	6.6818	1.7829	0.9879	0.0298	30.5188
$\gamma = 6$	3.2613	0.9433	0.9652	6.7456	1.8407	0.9876	0.0301	30.4363

Table 8. Quantitative results for SPOT-6 dataset with different numbers of outer iterations.

Case	SAM	Q4	Q	RASE	ERGAS	CC	RMSE	PSNR
$\gamma = 1$	6.8677	0.9109	0.9284	23.4889	4.8319	0.9803	0.0568	24.9167
$\gamma = 2$	3.6602	0.9270	0.9504	13.6097	3.1098	0.9824	0.0329	29.6569
$\gamma = 3$	2.8394	0.9287	0.9535	10.9922	2.6297	0.9824	0.0266	31.5123
$\gamma = 4$	2.6245	0.9268	0.9518	10.1182	2.5081	0.9819	0.0245	32.2318
$\gamma = 5$	3.2818	0.9300	0.9566	10.8640	2.6335	0.9843	0.0263	31.6141
$\gamma = 6$	3.8526	0.9295	0.9558	10.8789	2.6852	0.9841	0.0263	31.6022

From Table 5 to Table 8, quantitative results of the proposed method with γ changing from 1 to 6 are listed. When $\gamma = 1$, the proposed method essentially becomes Algorithm 1, which makes it convenient to compare it with the performance of Algorithm 2 directly. As expected, after combining Algorithm 1 with the iterative strategy, better quantitative performance is achieved, which can also be inferred from Figure 6.

202 In addition, we observe from Table 5 to Table 8 that the best quantitative performance is achieved when
 203 $\gamma = 5$. Generally speaking, the performance of Algorithm 2 rises as γ increases from 1 to 5, and begins to
 204 fall down at $\gamma = 6$. An exception can be noticed in the case of SPOT-6 dataset, where the best performance is
 205 observed at $\gamma = 4$. However, for the rest of the datasets, the case of $\gamma = 5$ outperforms other cases. Therefore,
 206 these results justify our choice of the value of γ .

207 Incidentally, we notice that the behavior of γ is similar to that in [56], whose output images begin to degrade
 208 if the outer iteration is not stopped properly. Therefore, we make a conjecture that the output of our iterative
 209 strategy gets too close to the blurred upsampling multispectral image when γ is larger than a threshold. Since the
 210 success of our iterative strategy has been preliminarily demonstrated by numerical results, an analysis of this
 211 conjecture can be explored in our future research.

212 4.4. Time Comparison with RKHS method

213 Since we mentioned in Section 3 that the proposed model is supposed to simplify model (3), it is reasonable
 214 to expect a reduction in running time when comparing these two methods. Time cost of both methods for the four
 215 datasets can be examined in Table 9. We point out that these results are obtained by running on the same laptop
 216 with 4GB RAM and 1.70GHz Intel(R) Core(TM) i5-4210U CPU as mentioned in the beginning of Section 4.

Table 9. Running time(s) of RKHS and the proposed method on four datasets

Method	Quickbird	Pléiades	WorldView-2	SPOT-6
RKHS	7263.22	27882.87	16559.93	31576.65
Proposed	207.71	851.11	512.47	863.59

217 From the table, it can be validated that the proposed method is much less time consuming than RKHS
 218 method, which means the goal of reduction in computational burden and running time is achieved.

219 5. Conclusions

220 In this paper, a new iterative pan-sharpening approach is proposed for the fusion of panchromatic image
 221 and multispectral image. The proposed variational model inherits the framework of RKHS method but is
 222 essentially different. Instead of paying attention to modelling the unknown high resolution multispectral image in
 223 a complicated way, we utilize framelet technique in image restoration for more effectiveness of regularization. An
 224 iterative scheme similar to [22] is also employed to improve performance of the proposed algorithm. Experiments
 225 on data from Quickbird, Pléiades, WorldView-2, and SPOT are conducted for visual and numerical assessment.
 226 The results demonstrate that the proposed method outperforms several state-of-the-art pan-sharpening methods
 227 both visually and quantitatively. Meanwhile, it succeeds in reducing time cost compared with RKHS method.

228 **Acknowledgments:** The authors would like to thank the supports by NSFC (61772003, 61702083) and Fundamental
 229 Research Funds for the Central Universities (ZYGX2016KYQD142, ZYGX2016J132, ZYGX2016J129).

230 **Author Contributions:** Liang-Jian Deng and Zi-Yao Zhang conceived and designed the experiments. Zi-Yao Zhang,
 231 Liang-Jian Deng and Chao-Chao Zheng wrote the source code. Zi-Yao Zhang performed the experiments and wrote the paper.
 232 Ting-Zhu Huang, Liang-Jian Deng, Jie Huang and Xi-Le Zhao provided detailed advice during the writing process. Ting-Zhu
 233 Huang and Liang-Jian Deng supervised the whole process and improved the manuscript.

234 **Conflicts of Interest:** The authors declare no conflict of interest.

235 References

1. Mohammadzadeh, A.; Tavakoli, A.; Valadan Zoej, M.J. Road extraction based on fuzzy logic and mathematical morphology from pansharpened IKONOS images. *Photogrammetric Record* **2006**, *21*, 44–60.
2. Souza Jr., C.; Firestone, L.; Silva, L.M.; Roberts, D. Mapping forest degradation in the Eastern Amazon from SPOT 4 through spectral mixture models. *Remote Sensing of Environment* **2003**, *87*, 494–506.
3. Carper, W.; Lillesand, T.; Kiefer, R. The use of intensity-hue-saturation transformations for merging SPOT panchromatic and multispectral image data. *Photogrammetric Engineering and Remote Sensing* **1990**, *56*, 459–467.

- 242 4. Chavez Jr., P.S.; Kwarteng, A.W. Extracting spectral contrast in Landsat thematic mapper image data using selective
243 principal component analysis. *Photogrammetric Engineering and Remote Sensing* **1989**, *55*, 339–348.
- 244 5. Laben, C.A.; Brower, B.V. Process for enhancing the spatial resolution of multispectral imagery using pan-sharpening,
245 2000. U. S. Patent 6011875.
- 246 6. Xu, Q.; Li, B.; Zhang, Y.; Ding, L. High-fidelity component substitution pansharpening by the fitting of substitution
247 data. *IEEE Transactions on Geoscience and Remote Sensing* **2014**, *52*, 7380–7392.
- 248 7. Kang, X.; Li, S.; Benediktsson, J.A. Pansharpening with Matting model. *IEEE Transactions on Geoscience and
249 Remote Sensing* **2014**, *52*, 5088–5099.
- 250 8. Shensa, M.J. The discrete wavelet transform: Wedding the à trous and Mallat algorithm. *IEEE Transactions on
251 Signal Processing* **1992**, *40*, 2464–2482.
- 252 9. Mallat, S. A theory for multiresolution signal decomposition: The wavelet representation. *IEEE Transactions on
253 Pattern Analysis and Machine Intelligence* **1989**, *11*, 674–693.
- 254 10. Nason, G.P.; Silverman, B.W., The Stationary Wavelet Transform and some Statistical Applications. In *Wavelets and
255 Statistics*; Springer New York, 1995; pp. 281–299.
- 256 11. Burt, P.J.; Adelson, E.H. The Laplacian pyramid as a compact image code. *IEEE Transactions on Communications*
257 **1983**, *COM-31*, 532–540.
- 258 12. Starck, J.L.; Fadili, J.; Murtagh, F. The undecimated wavelet decomposition and its reconstruction. *IEEE Transactions
259 on Image Processing* **2007**, *16*, 297–309.
- 260 13. Nencini, F.; Garzelli, A.; Baronti, S.; Alparone, L. Remote sensing image fusion using the curvelet transform.
261 *Information Fusion* **2007**, *8*, 143–156.
- 262 14. Price, J.C. Combining panchromatic and multispectral imagery from dual resolution satellite instruments. *Remote
263 Sensing of Environment* **1987**, *21*, 119–128.
- 264 15. Palsson, F.; Sveinsson, J.R.; Ulfarsson, M.O. A new pansharpening algorithm based on total variation. *IEEE
265 Geoscience and Remote Sensing Letters* **2014**, *11*, 318–322.
- 266 16. Zhao, X.L.; Wang, F.; Huang, T.Z.; Ng, M.K.; Plemmons, R. Deblurring and sparse unmixing for hyperspectral
267 images. *IEEE Transactions on Geoscience and Remote Sensing* **2013**, *51*, 4045–4058.
- 268 17. Fang, F.M.; Li, F.; Shen, C.M.; Zhang, G.X. A variational approach for pan-sharpening. *IEEE Transactions on Image
269 Processing A Publication of the IEEE Signal Processing Society* **2013**, *22*, 2822–2834.
- 270 18. Fang, F.M.; Li, F.; Zhang, G.X.; Shen, C.M. A variational method for multisource remote-sensing image fusion.
271 *International Journal for Remote Sensing* **2013**, *34*, 2470–2486.
- 272 19. He, X.; Condat, L.; Bioucas-Dias, J.; Chanussot, J.; Xia, J. A new pansharpening method based on spatial and spectral
273 sparsity priors. *IEEE Transactions on Image Processing* **2014**, *23*, 4160–4174.
- 274 20. Pan, Z.X.; Yu, J.; Huang, H.J.; Hu, S.X.; Zhang, A.W.; Ma, H.B.; Sun, W.D. Super-Resolution Based on Compressive
275 Sensing and Structural Self-Similarity for Remote Sensing Images. *IEEE Transactions on Geoscience and Remote
276 Sensing* **2013**, *51*, 4864–4876.
- 277 21. Masi, G.; Cozzolino, D.; Verdoliva, L.; Scarpa, G. Pansharpening by convolutional neural networks. *Remote Sensing*
278 **2016**, *8*, 594.
- 279 22. Deng, L.J.; Vivone, G.; Guo, W.H.; Mura, M.D.; Chanussot, J. A variational pansharpening approach based on
280 reproducible kernel Hilbert space and Heaviside function. *IEEE International Conference on Image Processing
(ICIP)*, 2017.
- 282 23. Aiazzi, B.; Baronti, S.; Selva, M. Improving Component Substitution Pansharpening Through Multivariate Regression
283 of MS + Pan Data. *IEEE Transactions on Geoscience and Remote Sensing* **2007**, *45*, 3230–3239.
- 284 24. Deng, L.J.; Guo, W.H.; Huang, T.Z. Single image super-resolution via an iterative reproducing kernel Hilbert space
285 method. *IEEE Transactions on Circuits and Systems for Video Technology* **2016**, *26*, 2001–2014.
- 286 25. Zhu, X.X.; Bamler, R. A Sparse Image Fusion Algorithm With Application to Pan-Sharpening. *IEEE Transactions
287 on Geoscience and Remote Sensing* **2013**, *51*, 2827–2836.
- 288 26. Dong, B.; Zhang, Y. An efficient algorithm for l_0 minimization in wavelet frame based image restoration. *Journal of
289 Scientific Computing* **2013**, *54*, 350–368.
- 290 27. Huang, J.; Donatelli, M.; Chen, R. Nonstationary Iterated Thresholding Algorithms for Image Deblurring. *Inverse
291 Problems and Imaging* **2013**, *7*, 717–736.
- 292 28. Cai, J.F.; Dong, B.; Shen, Z.W. Image restoration: a wavelet frame based model for piecewise smooth functions and
293 beyond. *Applied and Computational Harmonic Analysis* **2016**, *41*, 94–138.

- 294 29. Shi, Y.; Yang, X.; Cheng, T. Pansharpening of multispectral images using the nonseparable framelet lifting transform
295 with high vanishing moments. *Information Fusion* **2014**, *20*, 213–224.
- 296 30. Fang, F.M.; Zhang, G.X.; Li, F.; Shen, C.M. Framelet based pan-sharpening via a variational method. *Neurocomputing*
297 **2014**, *129*, 362–377.
- 298 31. Ron, A.; Shen, Z. Affine Systems in $L_2(\mathbb{R}^d)$: The Analysis of the Analysis Operator. *Journal of Functional Analysis*
299 **1997**, *148*, 408–447.
- 300 32. Dong, B.; Shen, Z. *MRA-based wavelet frames and applications*; IAS Lecture Notes Series, 2010.
- 301 33. Cai, J.F.; Osher, S.; Shen, Z.W. Split Bregman methods and frame based image restoration. *Multiscale Modeling and*
302 *Simulation: A SIAM Interdisciplinary Journal* **2009**, *8*, 337–369.
- 303 34. Elad, M.; Starck, J.; Querre, P.; Donoho, D. Simultaneous cartoon and texture image inpainting using morphological
304 component analysis (MCA). *Applied and Computational Harmonic Analysis* **2005**, *19*, 340–358.
- 305 35. Chambolle, A.; Pock, T. A First-Order Primal-Dual Algorithm for Convex Problems with Applications to Imaging.
306 *Journal of Mathematical Imaging and Vision* **2011**, *40*, 120–145.
- 307 36. He, B.; Tao, M.; Yuan, X. Alternating direction method with Gaussian back substitution for separable convex
308 programming. *SIAM Journal on Optimization* **2012**, *22*, 313–340.
- 309 37. Liu, J.; Huang, T.Z.; Selesnick, I.W.; Lv, X.G.; Chen, P.Y. Image restoration using total variation with overlapping
310 group sparsity. *Information Sciences* **2015**, *195*, 232–246.
- 311 38. Deng, L.J.; Guo, W.H.; Huang, T.Z. Single image super-resolution by approximated Heaviside functions. *Information*
312 *Sciences* **2016**, *348*, 107–123.
- 313 39. Ji, T.Y.; Huang, T.Z.; Zhao, X.L.; Ma, T.H.; Liu, G. Tensor completion using total variation and low-rank matrix
314 factorization. *Information Sciences* **2016**, *326*, 243–257.
- 315 40. Oden, J.T.; Glowinski, R.; Tallec, P.L. *Augmented Lagrangian and Operator Splitting Method in Non-linear*
316 *Mechanics*; Society for Industrial and Applied Mathematics, 1989.
- 317 41. Shi, W.; Ling, Q.; Yuan, K.; Wu, G.; Yin, W. On the Linear Convergence of the ADMM in Decentralized Consensus
318 Optimization. *IEEE Transactions on Signal Processing* **2014**, *62*, 1750–1761.
- 319 42. Donoho, D. De-noising by soft-thresholding. *IEEE Transactions on Information Theory* **1995**, *41*, 613–627.
- 320 43. Vivone, G.; Alparone, L.; Chanussot, J.; Dalla Mura, M.; Garzelli, A.; Licciardi, G.; Restaino, R.; Wald, L. A Critical
321 Comparison Among Pansharpening Algorithms. *IEEE Geoscience and Remote Sensing Letters* **2015**, *53*, 2565–2586.
- 322 44. Wald, L.; Ranchin, T.; Mangolini, M. Fusion of satellite images of different spatial resolutions: assessing the quality
323 of resulting images. *Photogrammetric Engineering and Remote Sensing* **1997**, *63*, 691–699.
- 324 45. Chavez Jr., P.S.; Sides, S.C.; Anderson, J.A. Comparison of three different methods to merge multiresolution and
325 multispectral data: Landsat TM and SPOT panchromatic. *Photogrammetric Engineering and Remote Sensing* **1991**,
326 *57*, 295–303.
- 327 46. Vivone, G.; Restaino, R.; Dalla Mura, M.; Licciardi, G.; Chanussot, J. Contrast and error-based fusion schemes for
328 multispectral image pansharpening. *IEEE Geoscience and Remote Sensing Letters* **2014**, *11*, 930–934.
- 329 47. Aiazzi, B.; Alparone, L.; Baronti, S.; Garzelli, A.; Selva, M. MTF-tailored multiscale fusion of highresolution MS
330 and PAN imagery. *Photogrammetric Engineering and Remote Sensing* **2006**, *72*, 591–596.
- 331 48. Zeng, D.; Hu, Y.; Huang, Y.; Xu, Z.; Ding, X. Pan-sharpening with Structural Consistency and $L_{1/2}$ Gradient Prior.
332 *Remote Sensing Letters* **2016**, *7*, 1170–1179.
- 333 49. Ghahremani, M.; Ghassemian, H. Nonlinear IHS: A Promising Method for Pan-Sharpening. *IEEE Geoscience and*
334 *Remote Sensing Letters* **2016**, *13*, 1606–1610.
- 335 50. Alparone, L.; Wald, L.; Chanussot, J.; Thomas, C.; Gamba, P.; Bruce, L.M. Comparison of pansharpening algorithms:
336 Outcome of the 2006 grs-s data-fusion contest. *IEEE Transactions on Geoscience and Remote Sensing* **2007**,
337 *45*, 3012–3021.
- 338 51. Wang, Z.; Bovik, C. A universal image quality index. *IEEE Signal Processing Letters* **2002**, *9*, 81–84.
- 339 52. Alparone, L.; Baronti, S.; Garzelli, A.; Nencini, F. A global quality measurement of pan-sharpened multispectral
340 imagery. *IEEE Geoscience and Remote Sensing Letters* **2004**, *1*, 313–317.
- 341 53. Choi, M. A new intensity-hue-saturation fusion approach to image fusion with a tradeoff parameter. *IEEE*
342 *Transactions on Geoscience and Remote Sensing* **2006**, *44*, 1672–1682.
- 343 54. Zhou, J.; Civco, D.L.; Silander, J.A. A wavelet transform method to merge Landsat TM and SPOT panchromatic data.
344 *International Journal of Remote Sensing* **1998**, *19*, 743–757.

- 345 55. Aiazzi, B.; Alparone, L.; Baronti, S.; Garzelli, A. Context-driven fusion of high spatial and spectral resolution
346 images based on oversampled multiresolution analysis. *IEEE Transactions on Geoscience and Remote Sensing* **2002**,
347 *40*, 2300–2312.
- 348 56. Osher, S.; Burger, M.; Goldfarb, D.; Xu, J.; Yin, W. An iterative regularization method for total variation-based image
349 restoration. *Multiscale Modeling and Simulation* **2005**, *4*, 460–489.

350 © 2018 by the authors. Submitted to *MDPI* for possible open access publication under the terms and conditions of the
351 Creative Commons Attribution (CC BY) license (<http://creativecommons.org/licenses/by/4.0/>).